coatings

MDPI

Article

Flow Field of Supersonic Oxygen Jet Generated by Various Wear Lengths at the Laval Nozzle Exit

Fuhai Liu [1,2], Songchao Lu [1,2], Sibao Zeng [3], Rong Zhu [2,4], Guangsheng Wei [2,4,*] and Kai Dong [2,4]

[1] National Center for Materials Service Safety, University of Science and Technology Beijing, Beijing 100083, China; liufuhaisteel@ustb.edu.cn (F.L.)
[2] Innovation Research Institute for Carbon Neutrality, University of Science and Technology Beijing, Beijing 100083, China
[3] Shiheng Special Steel Group Co., Ltd., Feicheng 271612, China
[4] Institute of Steel Sustainable Technology, Liaoning Academy of Materials, Shenyang 110167, China
* Correspondence: wgsustb2007@163.com

Abstract: As a main apparatus, the oxygen lance is used to deliver the oxygen element and transfer kinetic energy into the molten bath in the steelmaking process. However, the Laval nozzle exit would be gradually worn out during the service life, which suppresses the performance of the oxygen lance. This paper investigated three different wear length (L_w) conditions at the exit of the Laval nozzle through numerical simulations and high-temperature experiments with various oxygen flow rates. The result showed that the entrainment of the ambient gas was the key factor of the wear phenomenon for the Laval nozzle exit. The maximum total temperature of the gas phase at the Laval nozzle exit formed by the L_w of 0 mm, 2 mm, and 4 mm were 300 K, 959 K, and 1700 K, respectively. Thus, by increasing the L_w value, the total temperature of the gas phase was rapidly improved at the exit of the Laval nozzle, which further accelerated the wear phenomenon at the exit of the Laval nozzle. Besides, axial velocities at the end of the potential core formed by the L_w of 0 mm, 2 mm, and 4 mm were 483.7 m/s, 480.0 m/s, and 478.7 m/s, respectively. As a result, the wear phenomenon reduced the impaction ability of the oxygen jet, which suppressed the impaction depth and radius, resulting in a smaller droplet generation rate.

Keywords: Laval nozzle; wear; flow field; EAF

Citation: Liu, F.; Lu, S.; Zeng, S.; Zhu, R.; Wei, G.; Dong, K. Flow Field of Supersonic Oxygen Jet Generated by Various Wear Lengths at the Laval Nozzle Exit. *Coatings* **2024**, *14*, 1444. https://doi.org/10.3390/coatings14111444

Academic Editor: Cecilia Bartuli

Received: 17 October 2024
Revised: 11 November 2024
Accepted: 11 November 2024
Published: 13 November 2024

1. Introduction

As an important apparatus, the oxygen lance has a great effect on the oxygen utilization rate, temperature control, and impaction cavity shape in the steelmaking and refining process [1–3]. For further improving the dynamic and thermodynamic condition in a molten bath, the Laval nozzle is used to increase the initial velocity of the oxygen jet by converting its pressure energy into its kinetic energy. That means the structure of the Laval nozzle determines the process of controlling the oxygen lance to a certain extent [4,5]. During the service life in the EAF steelmaking process, the surface wall of the Laval nozzle would be gradually worn out. Thus, the Laval nozzle structure keeps changing with service time increasing, resulting in a reduction in the initial velocity of the oxygen jet and a suppression of the mixing effect in the molten bath. It is quite hard to directly measure the oxygen jet flow field during the steelmaking or refining process due to the high temperature and plenty of fumes in the furnace. Therefore, the numerical simulation and high-temperature experiment are carried out to analyze the behavior of the oxygen jet with various lance structures and operation methods [6–10].

Jia et al. [11] reported the jet characteristics of a double-structure oxygen lance by a series of numerical simulations and water experiments, and the result presented the double-structure design method can obviously improve the impaction ability of the oxygen jet, resulting in a better stirring effect of the molten bath. Liu et al. [12] introduced a method

to increase the initial velocity of an oxygen jet by preheating technology and found that the increasing rate of oxygen velocity was reduced by improving the oxygen temperature, and the impaction cavity formed by preheating method significantly increased comparing with the traditional oxygen supplement method. Odenthal [13] et al. researched the effect of the Laval nozzle structure on the oxygen jet flow field and proposed that the Laval nozzle designed by the characteristic-line method could transform the oxygen pressure energy into kinetic energy more effectively, resulting in the formation of a longer velocity potential core than the traditional Laval nozzle. Tang et al. [14] investigated the behavior of oxygen jets under various ambient temperatures and reported that the attenuation of coherent jet length was increased with decreasing ambient temperature. They also proposed the effect of fuel type on the shrouding combustion flame.

Feng et al. [15] found that the wear phenomenon at the exit of the Laval nozzle significantly reduced the velocity potential core of the oxygen jet under the same pressure conditions for the multi-nozzle lance, resulting in a decreased impaction area of the molten bath. Lv et al. [16] reported the effect of wear angle on the impaction ability of the supersonic oxygen jet, and the industrial application data showed that a low lance height can mitigate the influence of nozzle wear on the BOF steelmaking process. Garajau et al. [10] represented the temperature distribution at the outer wall surface temperature of the oxygen lance to demonstrate the reasons for Laval nozzle wear and concluded that optimizing the structural parameters of the Laval nozzle, along with avoiding post-combustion in its interior, can reduce the wear rate of the Laval nozzle exit.

In order to cope with the shortage of natural gas, some Chinese EAF planets use traditional oxygen lance instead of coherent oxygen lance. After a series of heats, the Laval nozzle exit shows signs of wear, which has an influence on the metallurgical indicator of this traditional oxygen lance. Therefore, researching the impact of wear length on the flow field of a supersonic oxygen jet can provide valuable insights into the operational procedure involved in the EAF steelmaking process. At present, although some literature reports the effect of various nozzle structure parameters and environmental conditions on the oxygen jet behaviors in the BOF steelmaking process, the behavior of oxygen jet formed by worn Laval nozzle in the EAF steelmaking process is quite few.

In this paper, both high-temperature experiment and numerical simulation will be carried out to investigate the effect of wear length at the Laval nozzle exit and oxygen flow rate on the flow field of supersonic oxygen jet generated by the traditional oxygen lance in the EAF steelmaking process. The axial velocity of the main oxygen jet at the centerline is measured in the high-temperature experiment to verify the accuracy of the simulation data. And the distribution of the velocity vector, impaction parameter, and droplet generation will be discussed to understand the effect of wear length on the behavior of the oxygen jet.

Based on this research, we will report on the wear phenomenon occurring at the exit of the Laval nozzle in the EAF steelmaking process, thereby supplementing the existing literature on the wear characteristics of top-blowing lances used in converters. Moreover, several recommendations have been proposed to enhance the service life of the side-blowing lance based on the behavior of the oxygen jet generated at varying wear lengths.

2. Laval Nozzle Structure and Experimental Measurement

In most Chinese steel plants, the one-dimensional isoentropic flow theory was still selected to process the Laval nozzle for the steelmaking process. In addition, a curve-line wall structure designed using the characteristics method was adopted in Europe and North America [13]. Based on the operational condition of 80 t EAF, the design flow rate, Mach number, and inlet oxygen temperature of the Laval nozzle were selected as 2000 Nm^3/h, 2.0, and 300 K, respectively. Then, the Laval nozzle parameters were achieved by the following equations [17]:

$$Q = 1.782 C_D \frac{A_t P_{in}}{\sqrt{T_{in}}} \quad (1)$$

$$\frac{A_e}{A_t} = \frac{1}{Ma}\left[\left(\frac{2}{\gamma+1}\right) \times \left(1 + \frac{\gamma-1}{2}Ma^2\right)\right]^{\frac{\gamma+1}{2(\gamma-1)}} \quad (2)$$

$$\frac{P_{out}}{P_{in}} = \left(1 + \frac{\gamma-1}{2}Ma^2\right)^{\frac{\gamma}{\gamma-1}} \quad (3)$$

where Q, P_{in}, and T_{in} are the flow rate ($Nm^3 \cdot min^{-1}$), inlet pressure (MPa), and temperature (K) of the oxygen gas, respectively. P_{out} and γ are the ambient pressure of 0.101 MPa and the specific heat ratio for oxygen of 1.4, respectively. A_t and A_e are the throat and exit areas (m^2) of the Laval nozzle, respectively. C_D is the oxygen utilization coefficient of 0.97. Thus, the design throat and exit radius of the initial Laval nozzle were 11.6 and 15.0 mm, respectively.

Figure 1 shows the schematic diagram of the initial and worn Laval nozzles. As reported by the previous literature [17–19], the wear was concentrated at the exit of the Laval nozzle. In order to investigate the effect of wear length on the flow field of an oxygen jet generated by a single Laval nozzle, the wear angle (α_w) was selected as 45°, and three types of wear length (L_w) were 0, 2, and 4 mm, respectively.

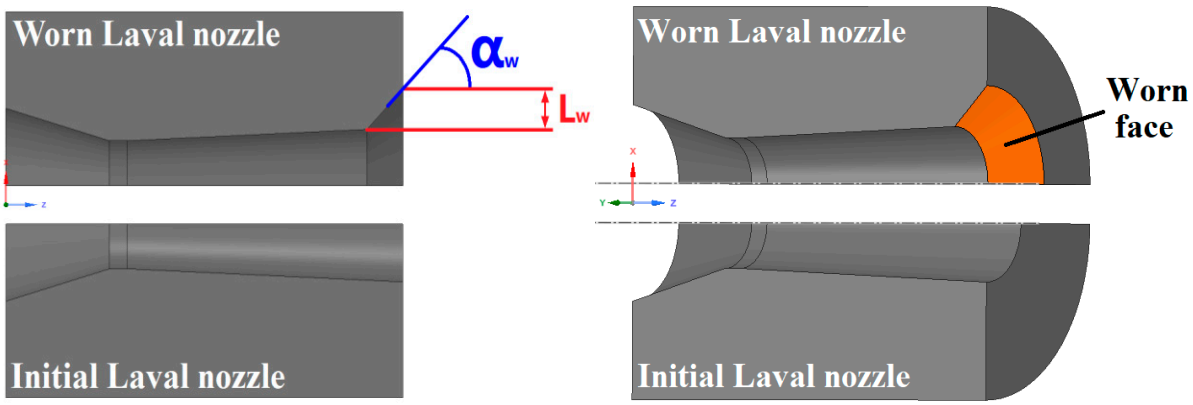

Figure 1. The schematic diagram of the initial and worn Laval nozzles.

Based on the operational conditions of the 80 t EAF, the flow rate of the side-blowing lance ranged from 1700 Nm^3/h to 2400 Nm^3/h to achieve an appropriate fluidity of the liquid slag. Therefore, this research selected flow rates of 1600 Nm^3/h, 2000 Nm^3/h, and 2400 Nm^3/h to investigate the effect of flow rate on the behavior of the oxygen jet at various L_w levels.

In this research, the design method of the initial Laval nozzle structure was the same, with the only difference being the wear length at the Laval nozzle exit. This meant that the variation of the Laval nozzle structure was generated by the wear of the nozzle tip. Additionally, the Laval nozzle structure used in both the numerical simulation and the experimental tests was the same, indicating that both the numerical simulation and the experimental tests were conducted using a full-scale industrial unit.

Figure 2 shows the schematic diagram of the experimental system. During the preparation phase, the burner was ignited to enhance the ambient temperature within the furnace. Twelve thermocouples were installed at various locations along the furnace's side wall. Once the ambient temperature reached 1700 K, the burner was extinguished. The Pitot tube was then positioned at specific points along the axial direction to measure the dynamic and static pressures of the oxygen jet at the centerline of the Laval nozzle, enabling the calculation of the jet's axial velocity. Subsequently, a thermocouple was placed at the same location to measure the total temperature of the oxygen jet. This indicated that the axial velocity of the oxygen jet was measured at the ambient temperature of 1700 K for comparison with simulation results.

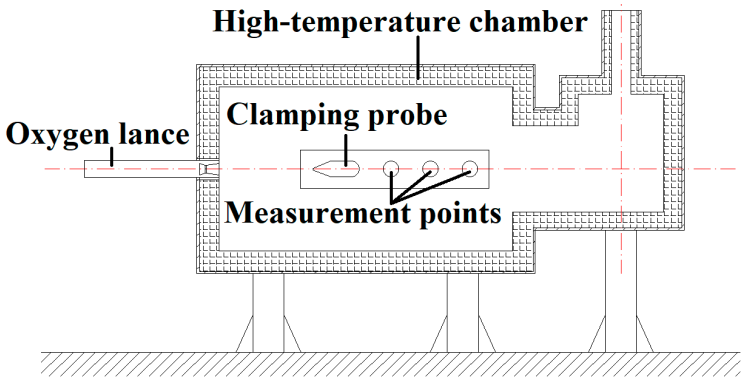

(**a**)

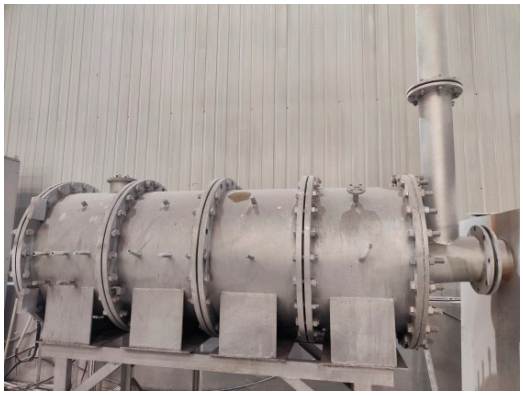

(**b**)

Figure 2. (**a**) The schematic diagram of the experimental system. (**b**) The high-temperature combustion furnace.

The axial velocity and total temperature of the oxygen jet were measured continuously over a duration of 20 s to calculate their average values. These measurements will subsequently be compared with simulation results to verify the accuracy of the numerical model. The details of the experimental system are also shown in Refs. [8,13,14], with only a brief description of its design provided here.

In this research, the ambient temperature in the experimental furnace was higher than the melting point of stainless steel. Therefore, both the oxygen lance and Pitot tube cooling water structure have been adopted to protect their design parameters from damage by the high-temperature burner. Equations (4) and (5) were used to calculate the axial velocity of the oxygen jet using the measurement data [18].

$$V_{O_2} = \sqrt{\frac{2\gamma RT}{\gamma - 1}\left[\left(\frac{p_d}{p_s}\right)^{(\gamma-1)/\gamma} - 1\right]},\ Ma > 0.3 \tag{4}$$

$$V_{O_2} = \sqrt{\frac{2(p_d - p_s)}{\rho_{O_2}}},\ Ma \leq 0.3 \tag{5}$$

where P_d and P_s are dynamic and static pressure (MPa) of the main oxygen jet, respectively. V_{O_2} and ρ_{O_2} are velocity ($m \cdot s^{-1}$) and density ($kg \cdot m^{-3}$) of the main oxygen jet, respectively. R is a constant of 8.314 $J \cdot mol^{-1} \cdot K^{-1}$.

3. Numerical Simulation Model

3.1. Governing Equation

To further investigate the behavior of the combined gas flow field, a simulation model was developed using Fluent software 2020 R2. During the simulation process,

Reynolds averaging was employed to solve the partial differential equations. The governing equations include the Navier–Stokes equations for continuity, momentum, and energy conservation, which are described as follows [19,20]:

Continuity equation:

$$\frac{\partial \rho}{\partial t} + \frac{\partial (\rho \overrightarrow{v_i})}{\partial x_i} = 0 \tag{6}$$

Momentum conservation equation:

$$\frac{\partial (\rho v_i)}{\partial t} + \frac{\partial (\rho v_i v_j)}{\partial x_j} = -\frac{\partial p}{\partial x_i} + \frac{\partial \left(\tau_{ij} - \rho \overline{v_i' v_j'} \right)}{\partial x_j} \tag{7}$$

Energy conservation equation:

$$\frac{\partial}{\partial t}(\rho E) + \frac{\partial}{\partial x_i}(\rho E v_i + p v_i) = -\frac{\partial}{\partial x_i}(q_i + C_P \rho_i \overline{v_i' T'}) + \frac{\partial (\tau_{ij} v_j - \rho_i \overline{v_i' v_j'} v_j)}{\partial x_i} + S_h \tag{8}$$

where v_i and v_j are the mean velocity ($\mathrm{m \cdot s^{-1}}$) components in the ith and jth directions, respectively. v_i' and v_j' are the fluctuating velocity ($\mathrm{m \cdot s^{-1}}$) components in the ith and jth directions, respectively. S_h stands for the volumetric heat ($\mathrm{W \cdot m^{-3}}$) source, and E and τ_{ij} are total energy (J) and viscous stress (Pa), respectively.

The SST *k-w* turbulence model was selected in the simulation process since it could accurately represent the diffusivity and dissipation of the supersonic jet [21]. Equations (9) and (10) represent the turbulence kinetic energy (k) and its dissipation rate (w) in the simulation model, as follows:

$$\frac{\partial}{\partial t}(\rho k) + \frac{\partial}{\partial x_i}(\rho k u_i) = \frac{\partial}{\partial x_j}(\Gamma_k \frac{\partial k}{\partial x_j}) + G_k - Y_k \tag{9}$$

$$\frac{\partial}{\partial t}(\rho w) + \frac{\partial}{\partial x_i}(\rho w u_i) = \frac{\partial}{\partial x_j}(\Gamma_w \frac{\partial w}{\partial x_j}) + G_w - Y_w \tag{10}$$

where G_k and G_w are the generation of turbulence kinetic energy ($\mathrm{m^{-2} \cdot s^{-2}}$) due to the mean velocity gradient and the generation of specific dissipation rate. Γ_k and Γ_w are the effective diffusivity of k and w, respectively. Y_k and Y_w are the dissipation of k and w, respectively.

3.2. Simulation Model Detail

Due to the axisymmetric of the supersonic oxygen jet flow field, a two-dimensional (2D) geometrical model with an axisymmetric method was built to investigate the behavior of the supersonic oxygen jet. The Laval nozzle and oxygen-flowing zone constituted the computational domain, considered 2.25 m downstream in the axial direction from the tip of the Laval nozzle and 0.45 m in the radial direction.

Based on the behavior of the oxygen jet, the velocity and pressure gradients were much bigger near the Laval nozzle exit than in the other regions. Therefore, the mesh density in this region has been improved, and the smallest mesh size was 0.05 mm × 0.05 mm. In order to enhance the accuracy of the simulation model, a wall boundary layer mesh has been built. The thickness of the first boundary layer mesh was 0.0005 mm, with a total of 10 layers of boundary mesh set. Based on the simulation results, the average y^+ of the first boundary layer mesh was 0.98, and the average cell equiangular skewness was 1.31×10^{-4}. Furthermore, only structured grids were employed in the mesh model.

As depicted in Figure 3, in the simulation model, the blue, red, and yellow lines represented the mass flow inlet, pressure outlet, and axis boundary conditions, respectively, while the other lines were defined as the wall boundary conditions. The origin point of the simulation model was established at the center of the Laval nozzle exit, as shown in Figure 3c.

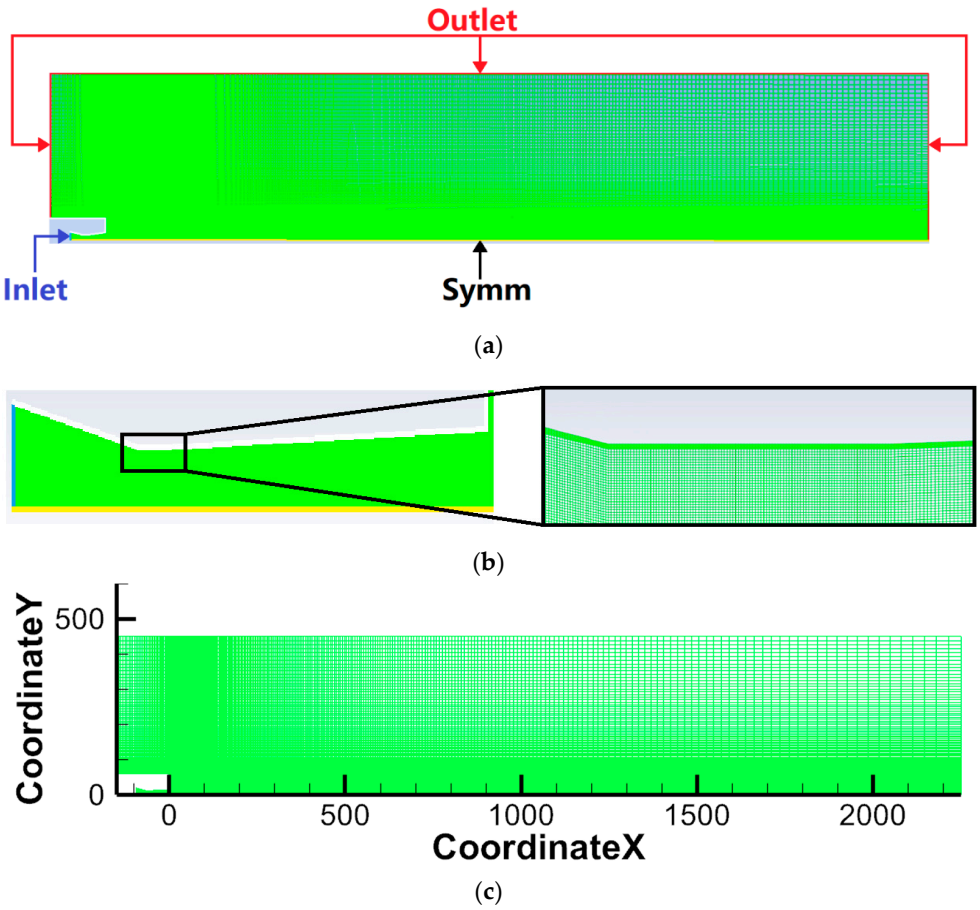

Figure 3. (**a**) The mesh and boundary condition distributions of the simulation model. (**b**) The mesh distributions of the Laval nozzle and its wall boundary layer. (**c**) The coordinate distribution of the simulation model.

At the solid impermeable wall, a non-slip condition and enhanced wall treatment were applied to this model. Initially, the computational domain started at rest with no oxygen blowing through the Laval nozzle, which was filled with static air. In the inlet position of Laval nozzles, the mass inlet boundary condition was adopted to inject the oxygen gas, and the pressure outlet was adopted as the boundary condition in the outlet position of the computational domain.

Table 1 presents the specifications of the boundary conditions, and the thermophysical properties of gases are shown in Table 2 [22]. In this paper, all the simulation results were achieved by using high-temperature conditions, according to the ambient temperature of 1700 K.

Table 1. Boundary conditions.

Name of Boundary	Type of Boundary Conditions	Values
Oxygen inlet	Mass flow rate (Nm^3/h)	1600/2000/2400
	Mach number	2.00
	Mass fractions (%)	O_2 = 100
	Oxygen temperature	300 K (27 °C)
Outlet	Static pressure (Pa)	101,325
	Mass fractions (%)	Air = 100
	Ambient temperature	1700 K (1427 °C)
Wall	Temperature	300 K (27 °C)

Table 2. Thermo-physical properties of three phases.

	Air	Oxygen Gas
Density/(kg·m^{-3})	Ideal gas	Ideal gas
Viscosity/(kg·m^{-1}·s^{-1})	$-0.13 + 7.94\cdot10^{-2}\cdot T - 7.17\cdot10^{-5}\cdot T^2 + 5.41\cdot10^{-8}\cdot T^3 - 2.21\cdot10^{-11}\cdot T^4 + 3.65\cdot10^{-15}\cdot T^5$	$-0.39 + 8.83\cdot10^{-2}\cdot T - 7.55\cdot10^{-5}\cdot T^2 + 5.51\cdot10^{-8}\cdot T^3 - 2.20\cdot10^{-11}\cdot T^4 + 3.59\cdot10^{-15}\cdot T^5$
Thermal conductivity/(W·m^{-1}·K^{-1})	$-0.77 + 1.10\cdot10^{-1}\cdot T - 8.29\cdot10^{-5}\cdot T^2 + 6.16\cdot10^{-8}\cdot T^3 - 2.47\cdot10^{-11}\cdot T^4 + 4.03\cdot10^{-15}\cdot T^5$	$-1.10 + 1.08\cdot10^{-1}\cdot T - 6.67\cdot10^{-5}\cdot T^2 + 4.60\cdot10^{-8}\cdot T^3 - 1.77\cdot10^{-11}\cdot T^4 + 2.81\cdot10^{-15}\cdot T^5$
C_p/(J·kg^{-1}·K^{-1})	$1.094 - 7.36\cdot10^{-4}\cdot T + 1.92\cdot10^{-6}\cdot T^2 - 1.76\cdot10^{-9}\cdot T^3 + 7.34\cdot10^{-12}\cdot T^4 - 1.18\cdot10^{-16}\cdot T^5$	$0.991 - 8.11\cdot10^{-4}\cdot T + 2.68\cdot10^{-6}\cdot T^2 - 2.91\cdot10^{-9}\cdot T^3 + 1.39\cdot10^{-12}\cdot T^4 - 2.48\cdot10^{-16}\cdot T^5$
Temperature/K	1700	300

Based on results reported in Refs. [11–15], the pure gas flow exhibits a stable flow state. Thus, the calculation was conducted in the steady solution mode, and the coupled method was adopted to solute the pressure–velocity coupling scheme [23,24].

The species transport model was selected to analyze the interaction between oxygen and nitrogen in the computational domain. The second-order discretization scheme was used for pressure and gas species discretization, and the least squares cell-based method was used for gradient discretization. Besides, the other variables (energy, turbulence kinetic energy, and dissipation rate) were solved by the QUICK scheme.

In this research, the solution convergence was selected as the average total temperature and velocity variations at the outlet of the computational domain were less than 1.0 K (1 °C) and 0.2 m/s, respectively. All simulations were conducted on a workstation configured with a 64-core CPU and 128 GB of RAM. After iterating for 12,000 steps, the simulation case achieved convergence, requiring an average processing time of 8 h.

3.3. Mesh Sensitivity

All simulations were performed on a workstation equipped with a 68-core CPU and 136 GB of memory. For the numerical models with three different L_w lengths, the average number of mesh elements was 73,200. When the models reached convergence, an average of 13,000 iterations was performed.

Figure 4 illustrates the axial velocity profiles derived from simulations conducted with three mesh levels: coarse mesh (34,400 cells), medium mesh (73,200 cells), and fine mesh (122,400 cells). Notably, the axial velocity variation between the medium and fine mesh levels is within 0.7%, indicating that the solution is relatively insensitive to grid refinement. In contrast, the variation between the coarse and medium mesh levels is approximately 4.3%. Consequently, the medium mesh level with 73,200 cells was chosen for the simulation to optimize computational efficiency.

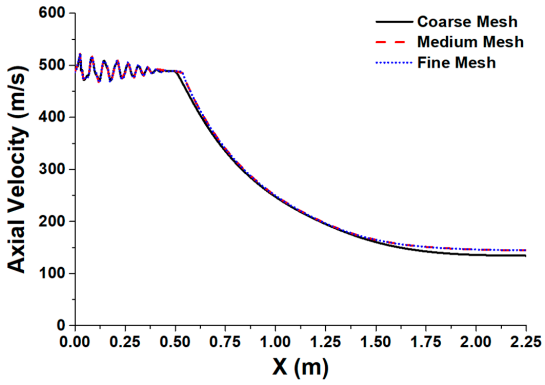

Figure 4. Axial velocity of coherent jet with three mesh levels.

4. Results and Discussions

4.1. Velocity Vector Distribution

During the steelmaking process, the high-temperature drop generated from liquid slag and molten bath will be splashed on the oxygen lance tip. The small-size high-temperature drop may be dragged to the surface wall of the Laval nozzle tip by the entrainment phenomenon. Then, the part of the solid copper at the tip region will be softened by overheating. As a result, the Laval nozzle structure might be destroyed, which generates the wear length at the Laval nozzle exit.

The extended section of the Laval nozzle is designed with a specific expansion angle to ensure the steady expansion of high-pressure oxygen. This configuration effectively converts the pressure potential energy of the oxygen jet into kinetic energy. However, wear occurring at the exit of the Laval nozzle can alter the structural parameters of the extended section.

As a result, the oxygen jet tends to expand along the worn areas of the Laval nozzle exit, as its static pressure exceeds that of the ambient gas. This paper analyzes the velocity vector of the oxygen jet to illustrate its expansion characteristics at the exit of the Laval nozzle under various operating conditions.

Figure 5 depicts the velocity vector distribution of the oxygen jet at the edge of the Laval nozzle tip with an oxygen flow rate of 2000 Nm^3/h. When the flow rate of the oxygen jet is constant, its pressure potential energy at the inlet of the Laval nozzle remains unchanged, provided that the same method of oxygen transport is utilized. This indicates that the initial expansion ability of the oxygen jet is determined by its flow rate. Thus, an expanding edge for the oxygen jet exists at the worn exit of the Laval nozzle, which extends further with an increased oxygen flow rate.

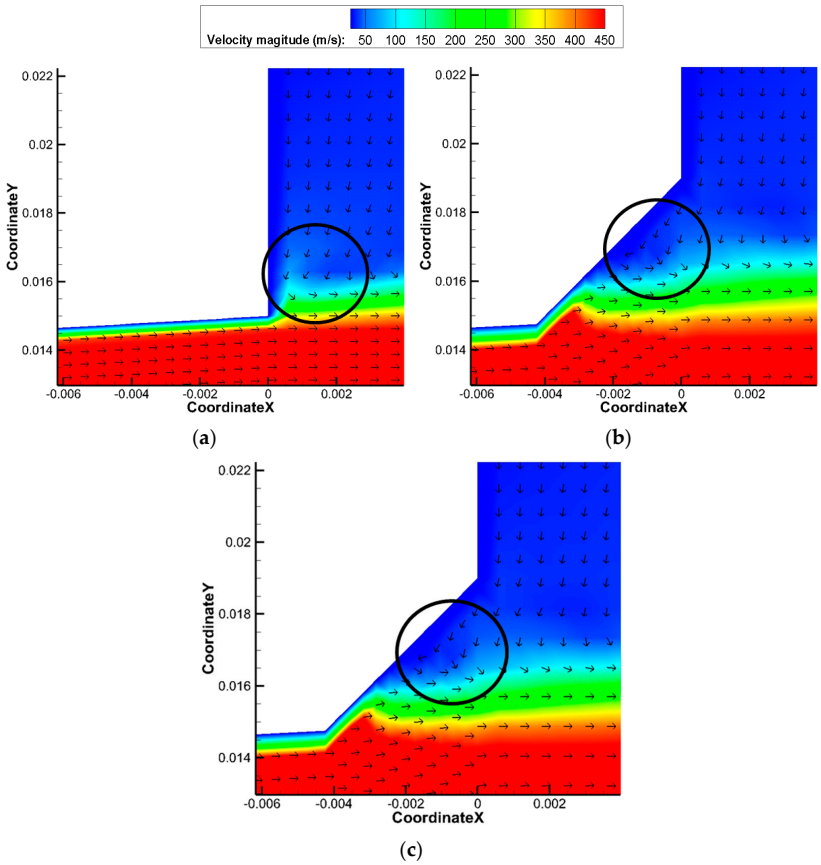

Figure 5. The velocity vector distribution of the oxygen jet at the edge of the Laval nozzle tip with an oxygen flow rate of 2000 Nm^3/h. (**a**) L_W = 0 mm. (**b**) L_W = 2 mm. (**c**) L_W = 4 mm.

Along this extending edge, the ambient gas will be entrained into the oxygen jet due to the velocity gradation, as shown in Figure 5a,b. Meanwhile, parts of the ambient air impact the surface wall of the Laval nozzle, as reflected in the velocity vector profile. This further proves that the small-size high-temperature drop may be dragged to the surface wall of the Laval nozzle tip by the entrainment phenomenon. As the wear length of the Laval nozzle exit increases, more gas flow is entrained into the worn region at the exit of the Laval nozzle.

In order to further investigate the effect of wear condition on the flow field at the exit of the Laval nozzle, the angles between the velocity vector of the oxygen jet and the positive *X*-axis and between the velocity vector of ambient gas and the positive *X*-axis have been measured, which are defined as $A_{o\text{-}x}$ and $A_{g\text{-}x}$, respectively, as represented in Figure 6a. According to the flow directions of the oxygen jet and ambient gas at the exit of the Laval nozzle, when the $A_{o\text{-}x}$ ranges from 0° to 90°, the oxygen jet shows an expansion phenomenon. Meanwhile, when the Ag-x ranges from 180° to 270°, the ambient gas is entrained into the oxygen jet.

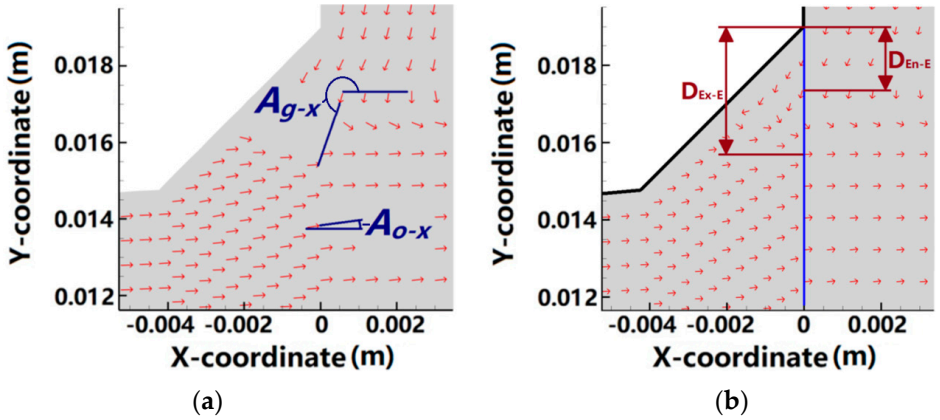

Figure 6. (**a**) The schematic diagram of the $A_{o\text{-}x}$ and $A_{g\text{-}x}$. (**b**) The schematic diagram of the $D_{Ex\text{-}E}$ and $D_{En\text{-}E}$.

For analyzing the interaction between the oxygen jet and ambient gas at the exit of the Laval nozzle, the biggest *X* coordinate is recorded when the $A_{o\text{-}x}$ ranges from 0° to 90°, and this *Y* coordinate is defined as the expansion point. Moreover, the smallest *Y* coordinate is also recorded at the exit of the Laval nozzle when the $A_{g\text{-}x}$ ranges from 180° to 270°, and this *Y* coordinate is defined as the entrainment point.

In addition, the distance between the expansion point (or entrainment point) and the *Y* coordinate for the edge of the Laval nozzle exit in the positive direction of the *Y*-axis is shortened as the $D_{Ex\text{-}E}$ (or $D_{En\text{-}E}$), as shown in Figure 6b.

Table 3 shows that the average $D_{Ex\text{-}E}$ are 4.5, 4.4, and 4.3 mm, respectively, when the oxygen flow rates are 1600, 2000, and 2400 Nm^3/h, ranging from L_w of 0 to 4 mm. Meanwhile, the average $D_{En\text{-}E}$ are 2.1, 1.6, and 1.5 mm, respectively, when the oxygen flow rates are 1600, 2000, and 2400 Nm^3/h, ranging from L_w of 0 to 4 mm. Thus, both $D_{Ex\text{-}E}$ and $D_{En\text{-}E}$ are decreased, with an improvement of the oxygen flow rate.

When the L_w are 0, 2, and 4 mm, the average $D_{Ex\text{-}E}$ values are 0.0, 4.9, and 8.4 mm, respectively, ranging from an oxygen flow rate of 1600 to 2400 Nm^3/h. As mentioned, the initial expansion ability of the oxygen jet is determined by the oxygen flow rate. As the length of the Laval nozzle increases, the cross-sectional area available for the entrainment of ambient gas into the wear region at the nozzle exit also increases, leading to a more pronounced entrainment phenomenon between the ambient gas and the oxygen jet. Consequently, a greater amount of kinetic energy from the high-velocity oxygen jet is transferred to the low-velocity ambient gas, thereby diminishing the expansion capability of the oxygen jet at the nozzle exit. This results in a shorter extending edge of the oxygen

jet. Thus, when the wear on the Laval nozzle intensifies, the oxygen jet will further expand at the exit of Laval, thereby increasing the $D_{Ex\text{-}E}$.

Table 3. The expansion and entrainment points at the Laval nozzle exit.

Label	Oxygen Flow Rate = 1600 Nm^3/h			Oxygen Flow Rate = 2000 Nm^3/h			Oxygen Flow Rate = 2400 Nm^3/h		
	L_w = 0 (mm)	L_w = 2 (mm)	L_w = 4 (mm)	L_w = 0 (mm)	L_w = 2 (mm)	L_w = 4 (mm)	L_w = 0 (mm)	L_w = 2 (mm)	L_w = 4 (mm)
Expansion point (mm)	15.0	12.0	10.3	15.0	12.1	10.7	15.0	12.2	10.9
$D_{Ex\text{-}E}$ (mm)	0.0	5.0	8.7	0.0	4.9	8.3	0.0	4.8	8.1
Entrainment point (mm)	——	14.8	14.9	——	15.4	15.7	——	15.6	16.0
$D_{En\text{-}E}$ (mm)	0.0	2.2	4.1	0.0	1.6	3.3	0.0	1.4	3.0

Based on the result, ranging from an oxygen flow rate of 1600 to 2400 Nm^3/h, the average $D_{Ex\text{-}E}$ values are 0.0, 1.7, and 3.5 mm for the L_w values of 0, 2, and 4 mm, respectively. The pressure potential energy of the oxygen jet increases with an elevated oxygen flow rate. Consequently, when the oxygen jet exits the Laval nozzle, its expansion ability is enhanced, which suppresses the entrainment phenomenon between the oxygen jet and the ambient gas in the wear region at the Laval nozzle exit. This effect causes the ambient gas to be displaced away from the central oxygen jet stream, thereby enlarging the expanding edge of the oxygen jet. Therefore, the average $D_{Ex\text{-}E}$ value increases with a higher oxygen flow rate.

As mentioned, the entrainment phenomenon may cause high-temperature ambient gas or slag droplets to impact the tip of the oxygen lance, leading to a wear phenomenon at the exit of the Laval nozzle, as depicted in Figure 5. To investigate the relationship between the entrainment phenomenon, oxygen flow rate, and L_w value further, the total temperature distributions at the exit of the Laval nozzle have been researched, as depicted in Figure 7.

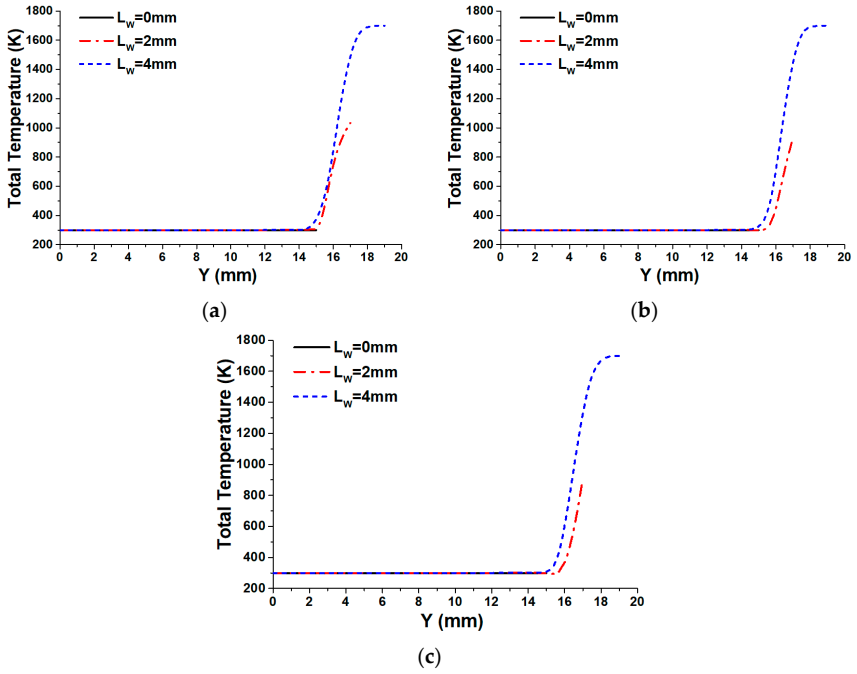

Figure 7. The total temperature distributions at the exit of the Laval nozzle with various conditions. (**a**) Oxygen flow rate = 1600 Nm^3/h. (**b**) Oxygen flow rate = 2000 Nm^3/h. (**c**) Oxygen flow rate = 2400 Nm^3/h.

Based on the result, with increasing the *Y* coordinate, the total temperature of the gas phase remains at 300 K, with the L_w value of 0 mm. This means that when the structure of the Laval nozzle is intact, no high-temperature ambient gas is entrained into the oxygen jet at the exit of the Laval nozzle. However, the high-temperature ambient gas still impacts the outer edge of the Laval nozzle exit, as shown in Figure 5a. As a result, the wear phenomenon is gradually formed.

With increasing the L_w value, the total temperature of the gas phase is rapidly improved after the *Y* coordinate reaches 14 mm. Meanwhile, the maximum total temperature of the gas phase is also obviously improved with a bigger L_w value. In this paper, when the gas phase reaches 310 K, its *Y* coordinate will be measured and addressed as the $Y_{T\text{-}310}$.

Table 4 shows that ranging from L_w of 0 to 4 mm, the average maximum total temperatures are 1011, 978, and 969 K, respectively, when the oxygen flow rates are 1600, 2000, and 2400 Nm^3/h. Meanwhile, the average $Y_{T\text{-}310}$ are 15.1, 15.3, and 15.5 mm, respectively, when the oxygen flow rates are 1600, 2000, and 2400 Nm^3/h, ranging from L_w of 0 to 4 mm. With a greater flow rate of the oxygen jet, the average maximum total temperature is increased, but the $Y_{T\text{-}310}$ is decreased.

Table 4. The maximum total temperature of the gas phase and $Y_{T\text{-}300}$ at the Laval nozzle exit.

Label	Oxygen Flow Rate = 1600 Nm^3/h			Oxygen Flow Rate = 2000 Nm^3/h			Oxygen Flow Rate = 2400 Nm^3/h		
	L_w = 0 (mm)	**L_w = 2 (mm)**	**L_w = 4 (mm)**	**L_w = 0 (mm)**	**L_w = 2 (mm)**	**L_w = 4 (mm)**	**L_w = 0 (mm)**	**L_w = 2 (mm)**	**L_w = 4 (mm)**
Max total temperature (K)	300	1034	1700	300	935	1700	300	908	1700
$Y_{T\text{-}310}$ (mm)	——	15.2	14.9	——	15.5	15.0	——	15.9	15.1

When the flow rate of the oxygen jet is increased, the pressure potential energy of the oxygen jet will be improved, resulting in a great expansion effect of the oxygen jet. Thus, the high-temperature ambient gas cannot easily be entrained into the Laval nozzle, which further reduces the total temperature at the edge of the Laval nozzle exit. As a result, the wall temperature of the Laval nozzle exit is decreased, which suppresses the wear phenomenon of the Laval nozzle. Based on the results, the oxygen lance should avoid the low-flow oxygen supply method during the steelmaking process.

Table 4 shows the maximum total temperature of the gas phase and $Y_{T\text{-}310}$ at the Laval nozzle exit.

As mentioned, when the L_w = 0 mm, the total temperature of the gas phase remains at 300 K at the Laval nozzle exit, resulting in no increase in total temperature. When the L_w values are 2 and 4 mm, the average maximum total temperatures are 959 and 1700 K, respectively. Besides, with the L_w values of 2 and 4 mm, the average $Y_{T\text{-}310}$ values are 15.5 and 15.0 mm, respectively.

When the L_w increases, more high-temperature ambient gas is entrained into the oxygen jet. Therefore, at the Laval nozzle exit, the outer temperature of the oxygen jet is rapidly enhanced, which also increases the surface temperature of the Laval nozzle. As a result, the mechanical property of Cu is reduced, and the wear phenomenon of the Laval nozzle exit is improved. Based on the result, the wear phenomenon of the Laval nozzle exit is increased by a lower oxygen jet flow rate and further deteriorates with a bigger L_w.

Meanwhile, an enhancement of the entrainment phenomenon of the ambient gas results in more ambient gas absorbing the kinetic energy from the oxygen jet, thereby reducing the impaction ability of the oxygen gas. The effect of oxygen flow rate on its impaction ability will be further discussed in Sections 4.2 and 4.3 by analyzing the velocity distribution of the oxygen jet and the theoretical impaction cavity shape of the molten bath.

4.2. Velocity Distribution

Figure 8 shows the axial velocity profiles of the main oxygen jet at the centerline with various conditions. The simulation results are shown by solid and dotted lines, whilst the measurement data are represented by various symbols (□, ◯ and △). In this paper, the ambient temperature in the tested condition is 1700 K for each case.

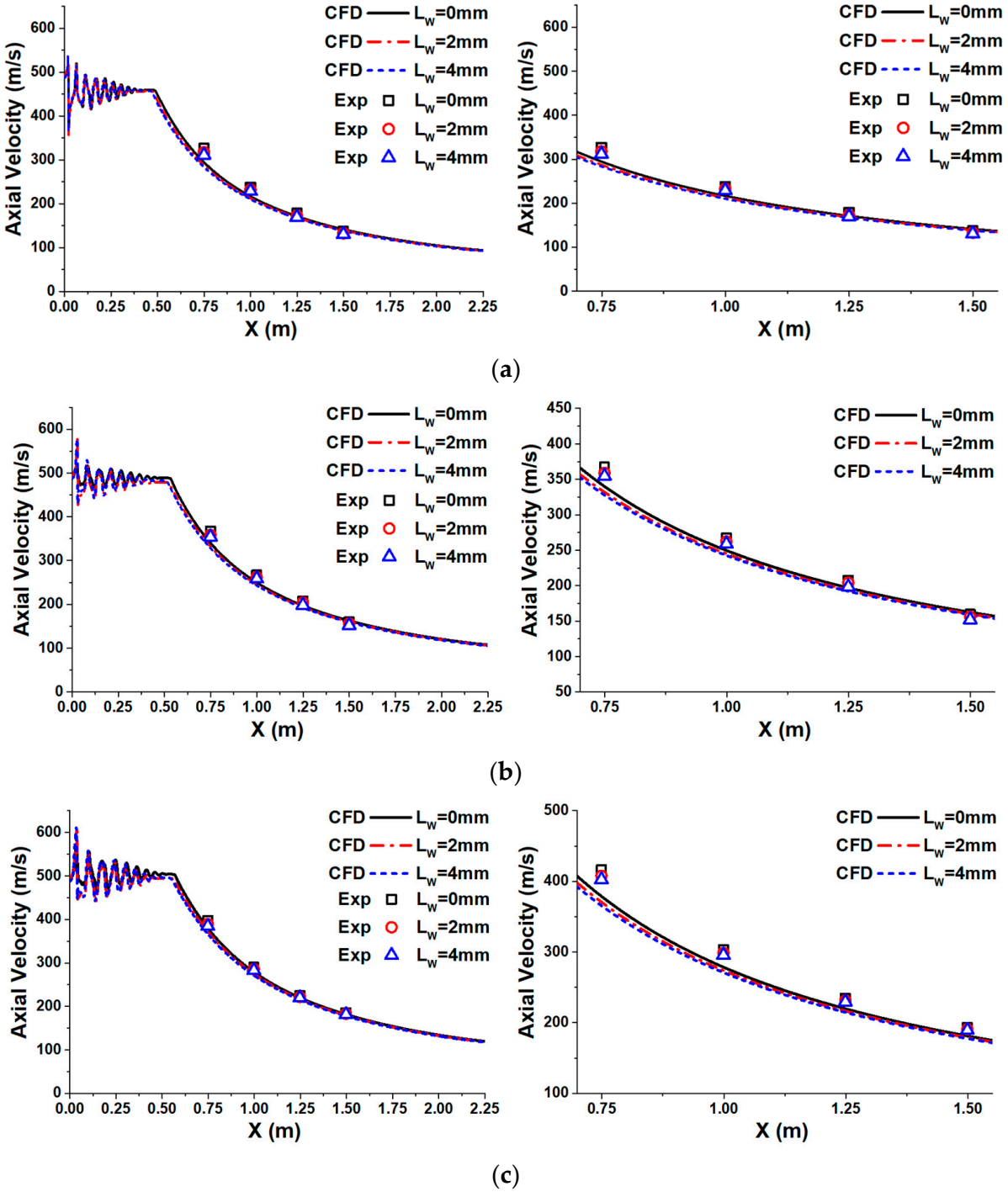

Figure 8. The axial velocity distribution of the main oxygen jet at the centerline with various conditions. (**a**) Oxygen flow rate = 1600 Nm^3/h. (**b**) Oxygen flow rate = 2000 Nm^3/h. (**c**) Oxygen flow rate = 2400 Nm^3/h.

The average axial velocity, illustrated in Figure 8, is derived from continuous measurements conducted over a duration of 20 s, as mentioned in Section 2. The experimental data indicate that the average fluctuation value of the measurement data is ±5.3% of its average value, with an average standard deviation of 10.5 m/s. This fluctuation value averages a cycle occurrence every 1.2 s.

Based on the result, the average variation of axial velocity between the simulation result and measurement data is 6.9%, which indicates that the experimental measurement data are in good agreement with that of the simulation results.

As shown in Figure 8, a shockwave of the main oxygen is generated immediately after the oxygen jet passes through the Laval nozzle exit. Subsequently, the intensity of the shockwave gradually reduces, leading to a constant axial velocity within a certain length along the centerline of the Laval nozzle. Finally, the axial velocity slowly decreases at the end of the velocity potential core. Based on the results, the initial axial velocity at the Laval nozzle exit is approximately 487 m/s for each case. The initial axial velocity variation caused by different oxygen flow rates or L w values is less than 1%, which can be considered negligible. This indicates that both the oxygen flow rate and L_w value have little influence on the initial axial velocity at the centerline of the Laval nozzle under the tested conditions.

However, the initial intensity of the shockwave shows a difference with the various L_w values at the same oxygen flow rate, which makes the axial velocity and the potential length of the main oxygen jet different. The maximum and minimum values of the axial velocity at the first shockwave for the main oxygen jet are represented as the V_{max} and V_{min}, respectively. The axial velocity fluctuation, calculated as the difference between V_{max} and V_{min}, is denoted as ΔV, as shown in Table 5.

Table 5. The axial velocity (m/s) of the main oxygen jet at the first shockwave.

Oxygen Flow Rate (Nm^3/h)	1600			2000			2400		
	V_{max}	V_{min}	ΔV	V_{max}	V_{min}	ΔV	V_{max}	V_{min}	ΔV
L_w = 0 mm	518	363	155	522	472	50	575	479	96
L_w = 2 mm	530	358	172	576	426	150	610	451	159
L_w = 4 mm	538	351	187	582	418	164	615	443	172

Based on the results, the V_{max} increases with increasing oxygen flow rate and L_w value. The V_{min} decreases with increasing L_w value, which is opposite to the effect of the oxygen flow rate. A larger ΔV value indicates a higher intensity of the shockwave, suggesting that more dynamic energy of the oxygen jet will be removed by the shockwave.

Therefore, the axial velocity of the main oxygen jet is reduced with a greater L_w value. And the ΔV value generated with the lower oxygen flow rate is the largest, followed by the higher oxygen flow rate, with the design oxygen flow rate exhibiting the lowest value. As mentioned in Section 4.1, the oxygen lance should avoid the low-flow oxygen supply method during the steelmaking process because this method can further increase the wear condition rate of the Laval nozzle exit and suppress the impaction ability of the main oxygen jet.

To further investigate the effect of L_w on the behavior of the first shockwave, the X coordinate of the main oxygen jet is recorded at the points where its velocity reaches both the maximum and minimum values, as shown in Table 6. In this paper, X-V_{max} and X-V_{min} represent the *X*-coordinates corresponding to the maximum and minimum velocities of the main oxygen jet, respectively. As mentioned, when the L_w increases, the intensity of the shockwave is enhanced. As a result, increasing the L_w value induces the shockwave phenomenon to occur earlier and achieves a smaller X-V_{max} and X-V_{min}.

Table 6. The *X* coordinate (mm) of the main oxygen jet at the first shockwave.

Oxygen Flow Rate (Nm^3/h)	1600		2000		2400	
	X-V_{max}	**X-V_{min}**	**X-V_{max}**	**X-V_{min}**	**X-V_{max}**	**X-V_{min}**
L_w = 0 mm	20.9	23.6	29.8	36.3	29.2	35.3
L_w = 2 mm	20.2	23.2	27.3	33.2	26.8	32.6
L_w = 4 mm	18.9	22.8	25.4	31.0	24.9	30.2

The design flow rate of the main oxygen jet is 2000 Nm^3/h. Thus, compared with the flow rates of 1600 Nm^3/h and 2400 Nm^3/h, the Laval nozzle can more efficiently convert the pressure potential energy of the jet into its kinetic energy with the flow rate of 2000 Nm^3/h, thereby suppressing the formation of shockwaves. Thus, both X-V_{max} and X-V_{min} generated by the main oxygen flow rate of 2000 Nm^3/h are greater than those produced at main oxygen flow rates of 1600 Nm^3/h and 2400 Nm^3/h.

When the flow rates of the main oxygen jet are 1600 Nm^3/h and 2400 Nm^3/h, the jet exhibits underexpansion and overexpansion phenomena, respectively. Thus, the shockwave is generated earlier at the 1600 Nm^3/h flow rate compared to the 2400 Nm^3/h flow rate. As a result, both X-V_{max} and X-V_{min} for the 2400 Nm^3/h flow rate are larger than those for the 1600 Nm^3/h flow rate.

To further investigate the oxygen flow field, both the potential core length and axial velocity have been researched at the end-point of the potential core. Table 6 shows the axial velocity potential core parameters with various conditions. The potential core lengths of the main oxygen jet using oxygen flow rates of 1600, 2000, and 2400 Nm^3/h are denoted as L_L, L_D, and L_H, respectively. The axial velocities at the end of the potential core using oxygen flow rates of 1600, 2000, and 2400 Nm^3/h are denoted as V_L, V_D, and V_H, respectively.

Table 7 shows that the axial velocity potential core length increases with a higher oxygen flow rate and a lower L_w value, which follows the same trend for the axial velocity at the end region of the potential core. The oxygen flow rates increased from 1600 Nm^3/h to 2000 Nm^3/h and from 2000 Nm^3/h to 2400 Nm^3/h, with the average length of the axial velocity potential core prolonging by 47.3 and 35.0 mm, respectively.

Table 7. The axial velocity potential core parameters with various conditions.

Lable	L_L	L_D	L_H	V_L	V_D	V_H
L_w = 0 mm	485 mm	532 mm	564 mm	459 m/s	488 m/s	504 m/s
Lw = 2 mm	473 mm	520 mm	555 mm	457 m/s	486 m/s	497 m/s
Lw = 4 mm	462 mm	510 mm	548 mm	456 m/s	484 m/s	496 m/s

The L_w increased from 0 mm to 2 mm and from 2 mm to 4 mm, with the average length of the axial velocity potential core decreasing by 11.0 and 9.3 mm, respectively. Hence, at the test condition, the increasing rate of length of the axial velocity potential core is decelerated with a greater oxygen flow rate, and the reducing rate of the length of the axial velocity potential core is also decelerated with a bigger L_w.

Meanwhile, the oxygen flow rate increased from 1600 Nm^3/h to 2000 Nm^3/h and from 2000 Nm^3/h to 2400 Nm^3/h, with the average axial velocity in the potential core improving by 28.7 and 13.0 m/s, respectively. In addition, the L_w increased from 0 mm to 2 mm and from 2 mm to 4 mm, with the average axial velocity in the potential core decreasing by 3.7 and 1.3 m/s, respectively. Thus, the increasing rate of average axial velocity in the potential core is decelerated with a greater oxygen flow rate, and the reducing rate of average axial velocity in the potential core is also decelerated with a bigger L_w, which is the same as the changing role of the average length of the axial velocity potential core.

As depicted in Figures 5 and 7, when the Lw increased, more high-temperature ambient gas was entrained into the oxygen jet, resulting in a higher total temperature at the periphery of the supersonic jet near the Laval nozzle exit. This indicates that the

entrainment phenomenon between the oxygen jet and ambient gas is strengthened, with a bigger L_w, which further intensifies the axial velocity fluctuation and a great shockwave intensity, as shown in Figure 8 and Table 5.

Based on the simulation result of axial velocity reported in Tables 5 and 7, there is more kinetic energy of the oxygen jet absorbed by the ambient gas when the Laval nozzle is worn. Meanwhile, the kinetic energy of the oxygen jet is further reduced when it passes through the shockwave. As a result, both the potential core length and velocity magnitude of the oxygen jet are suppressed, resulting in a lower impaction ability of the oxygen jet. Therefore, the research findings regarding the velocity distribution of the supersonic oxygen jet presented in this paper align with the reports in the Refs. [25–27].

4.3. Impaction Cavity Parameters and Droplet Generation Distributions

In the case of the side-blowing oxygen lance, the oxygen jet initially penetrates the flue gas before reaching the surface of the molten bath. This process generates an impaction cavity due to the total pressure gradient between the oxygen jet and the molten bath. As the impaction depth increases, a greater flow rate of the oxygen jet can directly react with the carbon in the molten steel, thereby enhancing the decarburization reaction rate and reducing smelting time. Furthermore, an enlarged impaction area increases the interface between the oxygen jet and the liquid slag, which consequently raises the (FeO) content in the liquid slag and improves the dephosphorization rate.

Therefore, it is important to estimate the effect of the wear length on the impaction cavity parameter. Based on the operational method of an 80 t EAF, the distance between the Laval nozzle tip and the surface of the molten bath is 1.4 m. In order to research the effect of oxygen flow rate and L_w on the impaction ability of the oxygen jet, the total pressure distribution at the lance height of 1.4 m has been represented in Figure 9.

As described, with a bigger L_w, both the shockwave intensity oxygen jet and entrainment phenomenon of ambient gas is improved, which obviously suppresses the impaction ability of the oxygen jet. Thus, the maximum total pressure of the oxygen jet at the lance height of 1.4 m is reduced with a bigger L_w. In addition, when the oxygen flow rate is increased, the initial kinetic energy of the oxygen jet gradually improved, resulting in a bigger total pressure, as shown in Figure 9. Refs [28,29] indicate that the impaction depth is increased with the total pressure of the oxygen lance, whereas the molten bath is included by two-layer liquid phases, which consist of liquid slag and molten steel. Thus, both the molten bath parameter and the total pressure of the oxygen jet are the main factors of the impaction cavity shape. Taking the two-layer liquid phases into consideration, the impaction depth of the molten bath can be calculated by the following equations:

$$H = \frac{P_t - P_a}{\rho_{slag} g},\ P_t < \rho_{slag} \cdot g \cdot H_{slag} \tag{11}$$

$$H = H_{slag} + H_{steel} = H_{slag} + \frac{(P_t - P_a) - \rho_{slag} g H_{slag}}{\rho_{steel} g},\ P_t \geq \rho_{slag} \cdot g \cdot H_{slag} \tag{12}$$

where H, H_{slag}, and H_{steel} are the impaction depth, liquid slag thickness, and penetrate depth of steel molten (m), respectively. P_t and P_a are the total pressure of the oxygen jet (Pa), and an atmospheric pressure of 101,325 Pa. g, ρ_{slag}, and ρ_{steel} are the gravitational acceleration of 9.81 m^2/s, liquid slag density (kg/m^3) and molten steel density (kg/m^3), respectively.

In this research, the density and thickness of liquid slag are assumed to be 3000 kg/m^3 and 0.15 m, respectively, and the molten steel density is 7000 kg/m^3. Hence, when the total pressure of the oxygen jet is equal to 103,532.3 Pa, the oxygen jet can penetrate 50 percent of the liquid slag thickness. The impaction radius is defined as the Y coordinate, where the total pressure of the oxygen jet is equal to 103,532.3 Pa. Figure 10 demonstrates the theoretical impaction depth and radius at the lance height of 1.4 m formed by various conditions.

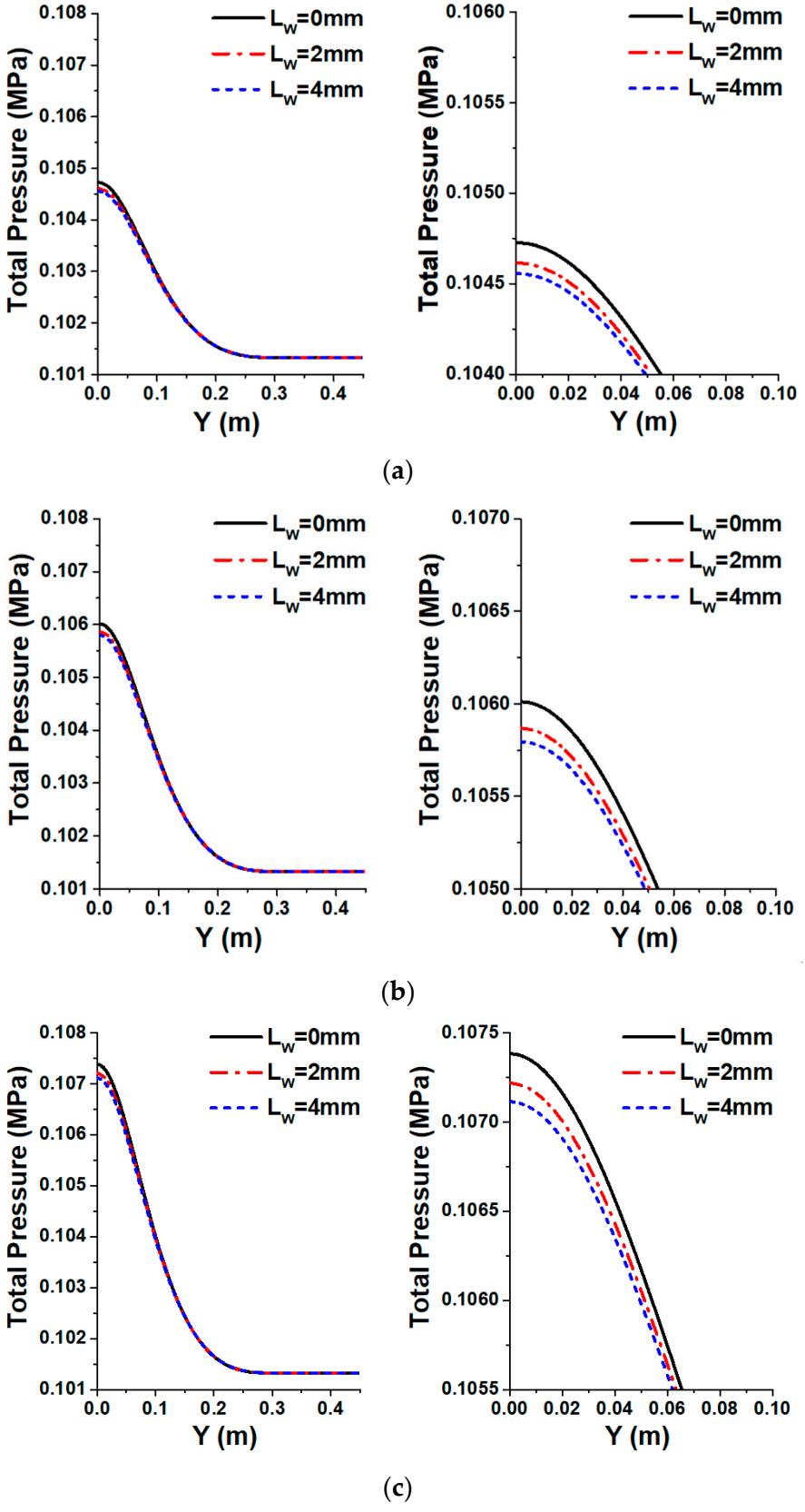

Figure 9. The total pressure distribution is at a lance height of 1.4 m under various conditions. (**a**) Oxygen flow rate = 1600 Nm^3/h. (**b**) Oxygen flow rate = 2000 Nm^3/h. (**c**) Oxygen flow rate = 2400 Nm^3/h.

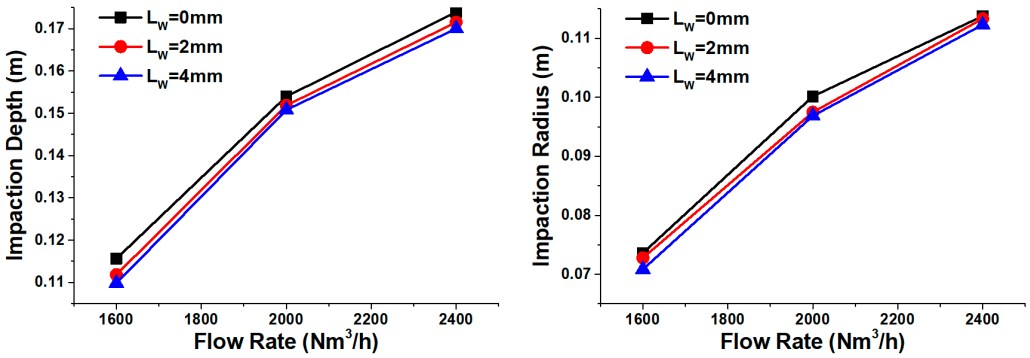

Figure 10. The theoretical impaction depth and radius at the lance height of 1.4 m are formed by various conditions. (**a**) Impaction depth. (**b**) Impaction radius.

Figure 10 depicts that both impaction depth and radius are increased with a greater oxygen flow rate but reduced with a bigger L_w. The oxygen flow rates increased from 1600 Nm^3/h to 2000 Nm^3/h and from 2000 Nm^3/h to 2400 Nm^3/h, with the average impaction depth increasing by 39.8 and 19.6 mm, respectively, and with the average impaction radius increasing by 25.7 and 15.0 mm, respectively, ranging from L_w of 0 to 4 mm.

The L_w increased from 0 mm to 2 mm and from 2 mm to 4 mm, with the average impaction depth decreasing by 2.8 and 1.5 mm, respectively, and with the average impaction radius increasing by 1.0 and 0.3 mm, respectively, ranging from the oxygen flow rate of 1600 Nm^3/h to 2400 Nm^3/h.

Thus, the increasing rate of impaction depth and radius is reduced with a greater oxygen flow rate and a bigger L_w. Compared with the impaction radius, the effects of oxygen flow rate and L_w on impaction depth are more prominent.

When the oxygen jet impacts the surface of the molten bath, it generates metal droplets, which increases the contact area between the oxygen jet and the molten bath. Consequently, this enhancement improves the oxygen mass transfer rate, further accelerating the reaction rate within the molten bath. In this study, the blowing number (N_B) proposed by Rout et al. [30] is employed to estimate the wear length related to the droplet generation rate in the steelmaking process, as expressed in the following equation:

$$N_B = \frac{\rho_g u_g^2}{2\sqrt{\rho_{steel}\sigma_{g\text{-}s}g}} \tag{13}$$

where ρ_g and u_g are the density (kg/m^3) and velocity (m/s) of oxygen gas, respectively. $\sigma_{g\text{-}s}$ is the surface tension between the oxygen gas and molten steel equal to 1.9 N/m. According to the N_B, the ratio of the droplets generated amount of (R_B) to the volumetric gas flow rate (F_G) can be calculated by the following equation:

$$\frac{R_B}{F_G} = \frac{N_B^{3.2}}{\left[2.6 \times 10^6 + 2.0 \times 10^{-4} \times N_B^{12}\right]^{0.2}} \tag{14}$$

Thus, the droplet generation rate is increased with a greater R_B/F_G. Based on the characteristics of the flow field, the R_B/F_G distribution at a lance height of 1.4 m with various conditions is presented in Figure 11.

Figure 11 presents the droplet generation rate increases with a greater oxygen flow rate and a smaller L_w. The oxygen flow rates increased from 1600 Nm^3/h to 2000 Nm^3/h and from 2000 Nm^3/h to 2400 Nm^3/h, with the average R_B/F_G increasing by 9.5 and 9.2 kg/Nm^3, respectively, ranging from L_w of 0 to 4 mm. It seems that although the increasing rate of R_B/F_G is reduced with a greater oxygen flow rate, the oxygen flow rate has a small effect on the R_B/F_G.

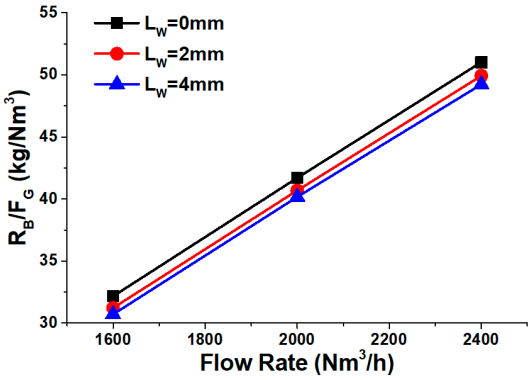

Figure 11. The R_B/F_G distribution is at a lance height of 1.4 m under various conditions.

Moreover, the L_w increased from 0 mm to 2 mm and from 2 mm to 4 mm, with the average R_B/F_G decreasing by 1.02 and 0.57 kg/Nm^3, respectively, ranging from an oxygen flow rate of 1600 Nm^3/h to 2400 Nm^3/h. Hence, the decreasing rate of R_B/F_G is reduced with a larger L_w. Based on the results, a higher oxygen flow rate and a smaller L_w can increase the droplet generation rate. This, in turn, enhances the contact area between the oxygen gas and the molten bath, resulting in a reduced oxygen supply time.

5. Conclusions

The cause of the Laval nozzle tip wear phenomenon and its influence on the oxygen jet flow field have been investigated in this paper. Both numerical simulation and experimental study have been carried out, and their results are in good agreement. The main conclusions of the present research can be summarized as follows:

(1) Based on the magnitude of ΔV, the intensity of the shockwave is improved by increasing the L_w and reducing the oxygen flow rate. Consequently, both the length of the velocity potential core and the impaction ability of the oxygen jet are reduced, which suppresses the impaction depth and radius, resulting in a smaller droplet generation rate;

(2) The average droplet generation rate, impaction depth, and impaction radius are decreased by 3.8%, 2.9%, and 2.6%, respectively, when the L_w is prolonged from 0 to 4 mm, ranging from an oxygen flow rate of 1600 to 2000 Nm^3/h. Thus, although the impaction ability of the oxygen jet is reduced by a longer wear length, the traditional oxygen lance with the L_w of 4 mm still exhibits good metallurgical performance in the EAF steelmaking process;

(3) When the worn area of the Laval nozzle has been observed, it is advisable to enhance the flow rate of the cooling water to extend the service life of the side-blowing oxygen lance. In addition, to maintain optimal dynamic conditions in the molten bath, the flow rate of the Laval nozzle should be gradually increased in response to the rising L_w;

(4) The wear phenomenon of the Laval nozzle first occurs at the edge of its exit. Consequently, a coating protection structure made of high-temperature resistant materials with good thermal conductivity and excellent thermal fatigue properties can be attempted at the edge of the Laval nozzle.

Author Contributions: Conceptualization, S.L. and F.L.; methodology, F.L.; software, S.L.; validation, K.D. and S.Z.; formal analysis, S.L.; investigation, S.L. and F.L.; resources, R.Z. and F.L.; data curation, S.Z.; writing—original draft preparation, S.L.; writing—review and editing, F.L. and G.W.; visualization, F.L. and R.Z.; supervision, F.L.; project administration, F.L. and R.Z.; funding acquisition, R.Z. and G.W. All authors have read and agreed to the published version of the manuscript.

Funding: This research was funded by the National Natural Science Foundation of China, grant numbers NSFC 52322407, NSFC 52074024 and NSFC 52274313.

Institutional Review Board Statement: Not applicable.

Informed Consent Statement: Not applicable.

Data Availability Statement: Data are contained within the article.

Conflicts of Interest: Author Sibao Zeng was employed by the company Shiheng Special Steel Group Co., Ltd. The remaining authors declare that the research was conducted in the absence of any commercial or financial relationships that could be construed as a potential conflict of interest.

List of Symbols

A_e	Exit area of the Laval nozzle (m^2)	A_t	Throat area of the Laval nozzle (m^2)
$A_{o\text{-}x}$	Angle between velocity vector of oxygen jet and the positive *X*-axis (°)	$A_{g\text{-}x}$	Angle between velocity vector of ambient gas and the positive *X*-axis (°)
α_w	Wear angle (°)	C_D	Oxygen utilization coefficient
$D_{Ex\text{-}E}$	Distance between the expansion point and the *Y* coordinate (mm)	$D_{En\text{-}E}$	Distance between the entrainment point and the *Y* coordinate (mm)
E	Total energy (J)	F_G	Volumetric gas flow rate ($Nm^3 \cdot s^{-1}$)
g	Gravitational acceleration ($m^2 \cdot s^{-1}$)	H	Impaction depth (m)
H_{slag}	Liquid slag thickness (m)	H_{steel}	Penetrate depth of steel molten (m)
k	Turbulence kinetic energy ($m^{-2} \cdot s^{-2}$)	L_w	Wear length (mm)
L_D	Potential core length of the main oxygen jet using an oxygen flow rate of 2000 Nm^3/h (mm)	L_H	Potential core length of the main oxygen jet using an oxygen flow rate of 2400 Nm^3/h (mm)
L_L	Potential core length of the main oxygen jet using an oxygen flow rate of 1600 Nm^3/h (mm)	N_B	Blowing number
P_a	Atmospheric pressure (MPa)	P_d	Dynamic pressure (MPa)
P_{in}	Inlet pressure of the Laval nozzle (MPa)	P_{out}	Ambient pressure (MPa)
P_s	Static pressure (MPa)	P_t	Total pressure of oxygen jet (Pa)
Q	Flow rate of the Laval nozzle ($Nm^3 \cdot min^{-1}$)	R	Gas constant
R_B	Droplet generation rate ($kg \cdot s^{-1}$)	S_h	Volumetric heat source($W \cdot m^{-3}$)
T_{in}	Inlet temperature of the Laval nozzle (K)	V_D	Axial velocity at the end of the potential core using an oxygen flow rate of 2000 Nm^3/h
V_H	Axial velocity at the end of the potential core using an oxygen flow rate of 2400 Nm^3/h	V_L	Axial velocity at the end of the potential core using an oxygen flow rate of 1600 Nm^3/h
V_{max}	Maximum axial velocity at the first shockwave for the main oxygen jet ($m \cdot s^{-1}$)	V_{min}	Minimum axial velocity at the first shockwave for the main oxygen jet ($m \cdot s^{-1}$)
ΔV	Axial velocity fluctuation is calculated as the difference between V_{max} and V_{min} ($m \cdot s^{-1}$)	V_{O_2}	Velocity of the main oxygen jet ($m \cdot s^{-1}$)
$X\text{-}V_{max}$	X-coordinates corresponding to the maximum velocity of the main oxygen jet (mm)	$X\text{-}V_{min}$	X-coordinates corresponding to the minimum velocity of the main oxygen jet (mm)
$Y_{T\text{-}310}$	Y coordinate with gas phase reaches at the 310 K (mm)	ρ_{O_2}	Density of the main oxygen jet ($kg \cdot m^{-3}$)
ρ_{slag}	Liquid slag density ($kg \cdot m^{-3}$)	ρ_{steel}	Molten steel density ($kg \cdot m^{-3}$)
Γ	Specific heat ratio of oxygen	v_i	Mean velocity component in the ith direction ($m \cdot s^{-1}$)
v_j	Mean velocity component in the jth direction ($m \cdot s^{-1}$)	v_i'	Fluctuating velocity ($m \cdot s^{-1}$) component in the ith direction

References

1. Liu, C.; Zheng, S.; Zhu, M. Variation in Multiphase Flow Characteristics by Single-Flow Post-combustion Oxygen Lance Blowing in BOF Steelmaking. *Metall. Trans. B.* **2023**, *54*, 1245–1261. [CrossRef]
2. Ramirez-Argaez, M.A.; Conejo, A.N. CFD Study on the Effect of the Oxygen Lance Inclination Angle on the Decarburization Kinetics of Liquid Steel in the EAF. *Metall. Res. Technol.* **2021**, *118*, 516. [CrossRef]
3. Dong, K.; Zhu, R.; Liu, F. Behaviours of supersonic oxygen jet with various Laval nozzle structures in steelmaking process. *Can. Metall. Q.* **2019**, *58*, 285–298. [CrossRef]
4. Liu, F.; Sun, D.; Zhu, R.; Li, Y. Characteristics of Flow Field for Supersonic Oxygen Multijets with Various Laval Nozzle Structures. Metall. *Metall. Trans. B* **2019**, *50*, 2362–2376. [CrossRef]
5. Zhou, X.; Ersson, M.; Zhong, L.; Yu, J.; Jönsson, P. Mathematical and Physical Simulation of a Top Blown Converter. *Steel Res. Int.* **2014**, *85*, 273–281. [CrossRef]
6. Feng, C.; Liu, F.; Zhu, R.; Dong, K.; Wei, G.; Tao, X. Flow Field Characteristic of Postcombustion Oxygen Lance Formed by Various Secondary Nozzle Arrangements. *Metall. Trans. B* **2024**, *55*, 600–611. [CrossRef]
7. Li, M.; Shao, L.; Li, Q.; Zou, Z. A Numerical Study on Particle-Induced Erosion to Laval Nozzle in Powder-Oxygen Injection Using BOF Lance. *JOM* **2021**, *73*, 2946–2952. [CrossRef]

8. Lv, M.; Zhu, R. Research on Coherent Jet Oxygen Lance in BOF Steelmaking Process. *Metall. Res. Technol.* **2019**, *116*, 502. [CrossRef]
9. Wei, G.; Zhu, R.; Cheng, T.; Dong, K.; Yang, L.; Wu, X. Effect of Main Gas Composition on Flow Field Characteristics of Supersonic Coherent Jets with CO_2 and O_2 Mixed Injection (COMI) at Steelmaking Temperature. *Metall. Trans. B* **2018**, *49*, 361–374. [CrossRef]
10. Silveira, G.F.; Lima, G.M.S.; Totti, M.B.; Roberto, C.P. Effects of Post Combustion Temperature on the Wear of the Supersonic Nozzles in BOF Lance Tip. *Eng. Fail. Anal.* **2019**, *96*, 175–185.
11. Jia, H.; Han, P.; Liu, K.; Li, Y.; Ba, K.; Feng, L. Characteristics of a Double-structure Oxygen Lance and Its Interaction with the Molten Pool in BOF Steelmaking. *AIP Adv.* **2021**, *11*, 085330. [CrossRef]
12. Zhao, F.; Liu, F.; Sun, D.; Zhu, R.; Dong, K. Behaviors of Supersonic Oxygen Multi-jets with Various Preheating Temperatures. *Metall. Trans. B* **2021**, *52*, 2626–2641. [CrossRef]
13. Odenthal, H.J.; Buess, S.; Starke, P.; Nörthemann, R.; Lohmeier, M. The new generation of SIS injector for improved EAF processes. In Proceedings of the METEC and 2nd European Steel Technology and Application Days (ESTAD), Düsseldorf, Germany, 15–19 June 2015.
14. Tang, G.; Chen, Y.; Silaen, A.K.; Krotov, Y.; Riley, M.F.; Zhou, C.Q. Effects of Fuel Input on Coherent Jet Length at Various Ambient Temperatures. *Appl. Therm. Eng.* **2019**, *153*, 513–523. [CrossRef]
15. Fen, C.; Zhu, R.; Han, B.; Yao, L.; Wu, W.; Wei, G.; Dong, J.; Jiang, J.; Hu, S. Effect of Nozzle Exit Wear on the Fluid Flow Characteristics of Supersonic Oxygen Lance. *Metall. Trans. B* **2020**, *51*, 187–199.
16. Lv, M.; Chen, S.; Li, H.; Guo, H.; Li, J.; Li, T. Effect of the Wear of Supersonic Oxygen Lance on the Stirring Characteristics and Metallurgical Effects in the Converter Steelmaking Process. *Ironmak. Steelmak.* **2023**, *50*, 235–243. [CrossRef]
17. Yuan, Z.; Pan, Y. *Oxygen Lance Technology for Steelmaking*, 1st ed.; Metallurgical Industry Press: Beijing, China, 2007.
18. Anderson, J.D. *Fundamentals of Aerodynamics*, 5th ed.; McGraw-Hill Education: New York, NY, USA, 2010.
19. Rezaei, H.; Rahimi, M.; Ovaysi, S.; Alsairafi, A.A. Computational Fluid Dynamics Modeling of Heat Transfer and Condensation in a Modified Laval Nozzle. *J. Thermophys. Heat Transf.* **2022**, *36*, 667–675. [CrossRef]
20. Launder, B.E.; Spalding, D.B. *Lectures in Mathematical Models of Turbulence*; Academic Press: Cambridge, UK, 1972.
21. Magnussen, B.F.; Hjertager, B.H. On Mathematical Modeling of Turbulent Combustion with Special Emphasis on Soot Formation and Combustion. *Combust. Inst.* **1976**, *15*, 719–729. [CrossRef]
22. Yaws, C.L. *Matheson Gas Data Handbook*, 7th ed.; Chemical Industry Press: Beijing, China, 2003.
23. Robert, B. Experimental investigation of the penetration of a high-velocity gas jet through a liquid surface. *J. Fluid Mech.* **1963**, *15*, 13–34.
24. Bode, M.; Gauding, M.; Goeb, D.; Falkenstein, T.; Pitsch, H. Applying Physics-informed Enhanced Super-resolution Generative Adversarial Networks to Turbulent Premixed Combustion and Engine-like Flame Kernel Direct Numerical Simulation Data. *Proc. Combust. Inst.* **2023**, *39*, 5289–5298. [CrossRef]
25. William, M.; Adrian, D.; Pravin, M.; Sumant, W. The Critical Role of Hydrogen in Linde's CoJet® Coherent Jet Technology. In Proceedings of the AISTech 2023—Proceedings of the Iron and Steel Technology Conference, Detroit, MI, USA, 8–11 May 2023.
26. Willian, D.R.; Totti, M.B. BOF Lance and Functions. In Proceedings of the AISTech 2022—Proceedings of the Iron and Steel Technology Conference, Pittsburgh, PA, USA, 16–18 May 2022.
27. Amano, S.; Sato, S.; Takahashi, Y.; Kikuchi, N. Effect of Top and Bottom Blowing Conditions on Spitting in Converter. *Eng. Rep.* **2021**, *3*, 12406. [CrossRef]
28. Qian, F.; Mutharasan, R.; Farouk, B. Studies of Interface Deformations in Single- and Multi-layered Liquid Baths Due to an Impinging Gas Jet. *Metall. Mater. Trans. B* **1996**, *27*, 911–920. [CrossRef]
29. Li, M.; Li, Q.; Kuang, S.; Zou, Z. Determination of Cavity Dimensions Induced by Impingement of Gas Jets onto a Liquid Bath. *Metall. Mater. Trans. B* **2016**, *47*, 116–126. [CrossRef]
30. Rout, B.K.; Brooks, G.; Subagyo, E.; Rhamdhani, M.A.; Li, Z. Modeling of Droplet Generation in a Top Blowing Steelmaking Process. *Metall. Mater. Trans. B* **2016**, *47*, 3350–3361. [CrossRef]